High Resolution Wideband Imaging of Fast Rotating Targets Based on Random PRI Radar

Zhen Liu*, Xin Chen, and Jinping Sui

Abstract—By exploiting the micro-motion features of fast rotating targets, wideband radar has been successfully applied to high resolution imaging. However, due to the traditional fixed pulse repetition interval (PRI), the target image may suffer from aliasing in some practical situations. In this paper, under the compressed sensing (CS) radar framework, an efficient wideband imaging scheme with random PRI signal is introduced for aliasing reduction. Considering that direct application of the CS theory will result in large-scale dictionaries and high computational complexity, we firstly generate a low resolution image by applying modified generalized Radon transform on range-slow time domain and then scale down the dictionary column by reserving the atoms corresponding to those strong scattering areas. Simulation results show that this scheme can achieve aliasing-free images with acceptable computational cost.

1. INTRODUCTION

As an effective remote sensing technology, wideband radar imaging has been widely used in many military and civilian applications such as target recognition. In order to reveal the geometric structure and size for those fast rotating targets including space debris, flying missiles, airscrews of airplane, etc., high resolution two-dimensional (2-D) imaging is always performed by exploiting their micro-motion features. For traditional wideband radar with fixed pulse repetition interval (PRI), the high resolution range profiles (HRRPs) of a rotating scatterer exhibit sinusoidal modulus and phase in the range-slow time domain. In order to image fast rotating targets, the curve estimation algorithms such as generalized Radon transform (GRT) [1], extended Hough transform (EHT) [2] and real-valued inverse Radon transform (RIRT) [3] are successfully applied to noncoherent integration along the slow time. Additionally, some coherent algorithms such as complex-valued back-projection (CBP) [4], complex-valued inverse Radon transform (CIRT) [3] and segmental pseudo Keystone transform (SPKT) [5] are proposed to achieve higher resolution.

Although there are so many efficient algorithms of rotation target imaging, for some practical applications, due to the fixed PRI (FPRI) in traditional radar scheme, the target image may suffer from aliasing when the rotation frequency is too large to satisfy the conditions of pulse repetition frequency (PRF) proposed in [3] for CIRT or in [6] for EHT. As this phenomenon is more likely to happen for fast rotating targets in low PRF radar, how to reduce aliasing in target imaging requires further investigation.

In fact, it is well known that the aliasing is mainly caused by the long FPRI, which is equivalent to uniform undersampling. Therefore, the random PRI (RPRI) radar, which has already been alluded to in the past [7–10] for smearing the ambiguity peaks, is also a candidate for wideband imaging of fast rotating targets. However, due to uncertainty principle in RPRI signal processing, the non-parametric approaches such as CBP suffer from global leakage problems, which will lead to high

sidelobe pedestal. Since random or irregular undersampling combined with the compressed sensing (CS) theory [11–13] provides a preferable approach for aliasing-free spectral analysis [14, 15] with low sidelobe and high resolution, the recent signal processing methods for RPRI radar is also under the CS framework. For example, in [16] the random slow time undersampling and jittered slow time undersampling are introduced for the CS-based cross-range compression in synthetic aperture radar (SAR) imaging. In [17, 18], we have proposed the CS-based algorithm to successfully resolve the velocity ambiguity for moving target detection in the RPRI pulse-Doppler radar.

Following this idea, we have tried to apply the CS framework to aliasing reduction in high resolution imaging of fast rotating targets by applying the RPRI signal. In addition, considering that the direct application of CS theory will result in large-scale dictionaries and high computational complexity, we intended to scale down the dictionaries by using some prior information. It is well known that the existing CS-based schemes mainly focus on the undersampling of the measurement data [16, 19–22], which will reduce the row number of the dictionary. For our problem, we also thin the dictionary in the parameter domain, which determines its column number. In [23], a scale-down-dictionary compressed sensing (SDD-CS) scheme for narrowband RPRI radar is presented, in which the short-time compressed sensing (STCS) algorithm proposed in [24] is applied to generate the aliasing-free TFD of the echo signals, and the modified GRT (MGRT) is applied for noncoherent integration of the sine curves on the TF domain to obtain the target image of low resolution. Then the strong scattering areas are extracted to form proper dictionaries, based on which the well-focused images with almost no aliasing can be achieved efficiently.

In this paper, we present a similar scheme for wideband RPRI radar. Firstly, MGRT is also applied to noncoherent integration of the sine curves along the random slow time to obtain the target image of low resolution, then the dictionary forming and SDD-CS-based imaging can be done in a similar way. The paper is organized as follows. In Section 2, the aliasing micro-Doppler effect of rotation is introduced briefly, and the signal model of fast rotating target in wideband RPRI radar is formed. Then the SDD-CS processing scheme for wideband RPRI radar is detailed in Section 3, in which the MGRT for the range-random slow time domain is introduced and the procedure of dictionary formation is given. In Section 4, some complementary issues such as the resolution performance and computational complexity are further analyzed. Section 5 carries out some numerical simulations to testify the performance of SDD-CS for wideband RPRI radar. Finally, conclusions are made in Section 6.

2. WIDEBAND SIGNAL MODEL FOR FAST ROTATING TARGETS IN RPRI RADAR

2.1. Micro-Doppler Effects of Rotation and Aliasing

In this paper, we will focus on the fast rotational targets such as space debris, flying missiles or airscrews of airplane. Suppose that the target can be modeled as K ideal point scatterers rotating uniformly around the imaging center O, as shown in Fig. 1. The distance from target center to radar is R_0 and the target translational motion is assumed to have been compensated for completely.

During the coherent processing interval (CPI) which is longer than one rotation period so that the rotation rate can be estimated by autocorrelation, the instantaneous rotation angle of target is defined as $\Delta\theta(t)$, and the instantaneous range from the kth scatterer at (x_k, y_k) to radar is given by

$$\begin{aligned} R_k(t) &= R_0 + y_k \cos \Delta\theta(t) + x_k \sin \Delta\theta(t) \\ &= R_0 + y_k \cos \omega t + x_k \sin \omega t \end{aligned} \tag{1}$$

where $\omega = 2\pi f_{rot}$ stands for the rotation rate, then the micro-Doppler frequency of the radar echo signal from the kth point scatterer is time dependent and can be modeled as

$$f_k(t) = \frac{2f_c}{c} \frac{dR_k(t)}{dt} = \frac{2f_c\omega}{c}(y_k \sin \omega t - x_k \cos \omega t) \tag{2}$$

in which f_c is the carrier frequency and c the speed of light.

In traditional FPRI radar with PRI T_r, the time-varying micro-Doppler frequency can be regarded as being uniformly sampled, and the maximum unambiguous Doppler frequency is equal to the sampling rate as $1/T_r$. It has already been pointed out in [23] that when the required PRI cannot be satisfied,
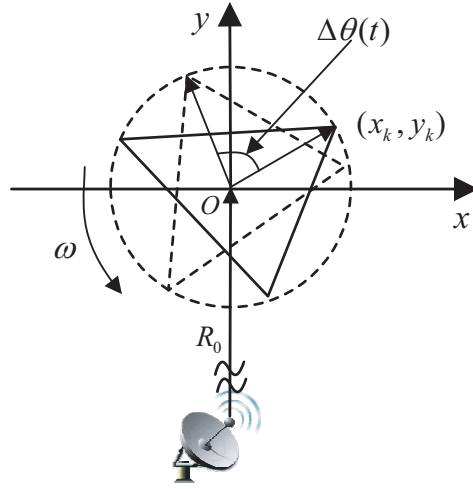
Figure 1. Geometry scenes for radar imaging of fast rotating targets.

spurious scatterers will appear in the corresponding radar images, especially for those complex targets where interference among scatterers is serious. Therefore, the RPRI radar is applied in the following analysis to reduce aliasing.

2.2. Signal Model in RPRI Radar

As shown in Fig. 2, in RPRI radar with random jittering in slow time, we transmit N chirp pulses at $T_n = nT_r + \Delta T_n$ ($\Delta T_0 = 0$, $n = 0, 1, \ldots, N-1$) in the CPI $(0, NT_r)$, where T_r is the average PRI, and ΔT_n are distributed randomly within $(0, T_r)$. Suppose that a single transmitted chirp pulse is

$$s(\tau) = A \cdot \text{rect}\left(\frac{\tau}{T}\right) \cdot \exp\left[j2\pi\left(f_c\tau + \frac{\gamma}{2}\tau^2\right)\right] \tag{3}$$

where τ is the fast time, A the signal amplitude, γ the chirp rate, T the time width of chirp pulse, and $\text{rect}(\tau/T)$ the unit rectangular function.
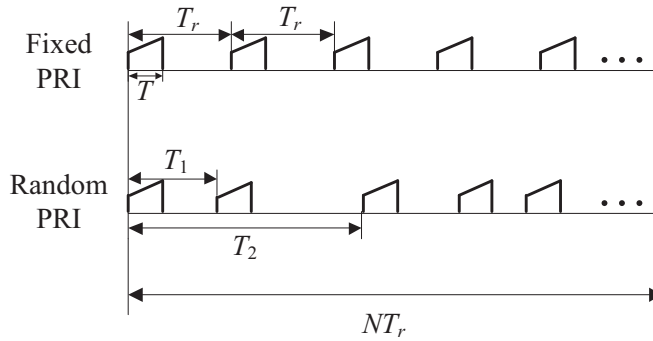

Figure 2. The fixed and random PRI pulse train.

For the rotational target with K scatterers in Fig. 1, based on the far field and "stop-and-go" assumption, the complex envelope of the echo signal can be written as

$$s_r(\tau, T_n) = \text{rect}\left(\frac{T_n}{NT_r}\right) \cdot \sum_{k=1}^{K} A_k \cdot \text{rect}\left(\frac{\tau - 2R_k(T_n)/c}{T}\right)$$

$$\cdot \exp\left\{j2\pi\left[f_c\left(\tau - \frac{2R_k(T_n)}{c}\right) + \frac{\gamma}{2}\left(\tau - \frac{2R_k(T_n)}{c}\right)^2\right]\right\} \tag{4}$$

where A_k is the backward scattering amplitude of the kth scatterer. After range compression of each echo pulse by dechirping and removing the residual video phase, (4) becomes

$$s_r(r, T_n) = \sum_{k=1}^{K} A_k \cdot B \cdot \text{sinc}\left[\frac{2B}{c}(r - r_k(T_n))\right] \cdot \exp\left(-j4\pi f_c \frac{r_k(T_n)}{c}\right) \tag{5}$$

where the support range of r is $[-r_{\max}, r_{\max}]$, and $B = T\gamma$ is the signal bandwidth, $r_k(t) = y_k \cos \omega t + x_k \sin \omega t$. It can be seen that for a rotating target with several ideal scattering canters, its echo signal in the $\tau - T_n$ domain is superposition of components with both sinusoidal modulated modulus and phase. In practice, when $B \geq c/(4r_{\max})$, one or more sinusoids will have larger amplitudes than half of the range resolution and the corresponding curves will appear as sinusoids on the range-slow time plane, which is actually a special kind of migration through resolution cells (MTRC) [25]. In this situation, the radar is regarded as the wideband one, which is focused in this paper.

Provided that the imaging interval is longer than one rotation period so that the rotation rate can be estimated, the high resolution images can still be obtained by the CBP approach [4, 26]. Owing to the randomness of slow time, the aliasing effect will be well suppressed even under lower average PRF. However, due to the uncertainty principle, they will suffer from global leakage problems, which will lead to high sidelobe pedestal. Therefore, in the following two sections, we intend to investigate new algorithms to generate aliasing-free high resolution images with low sidelobe.

3. WIDEBAND RPRI RADAR IMAGING BASED ON SDD-CS

3.1. Low Resolution Imaging by MGRT

For wideband RPRI radar, the positions of all scatterers can be estimated by detecting the random-sampling sine curves in the range-slow time domain, which is the same as the detection of a specific curve in the area of digital image processing. Since the widely-used discrete GRT algorithm [27] can convert a difficult global detection problem in the image domain into a more easily solved local peak detection problem in the parameter domain, here we will modify it for the range-slow time image with random sampling in slow time so that the range variation of each scatterer can be correctly traced, and its position parameters can be estimated.

Assume that the range sampling interval is $\Delta r \leq c/(2B)$ and that the range domain of the HRRPs is $R = (M - 1)\Delta r \geq 2r_{\max}$ with M range cells, then the discrete image can be represented as $d(m, n) = |s_r(r_m, T_n)|$ and the correspondence between the discrete image domain indices (m, n) and the variables (r_m, T_n) can be written as

$$r_m = -R/2 + m\Delta r, \quad m = 0, \ldots, M - 1 \tag{6}$$
$$T_n = nT_r + \Delta T_n, \quad n = 0, \ldots, N - 1 \tag{7}$$

Suppose that the transformation curve is $\phi(t; \xi)$, then the MGRT of the discrete image $d(m, n)$ can be defined as

$$D(\xi) = \sum_{n=0}^{N-1} d(\phi_d(n; \xi), n) \tag{8}$$

with n corresponding to the random slow time T_n and $\phi_d(n; \xi) = \text{round}(\frac{\phi(T_n; \xi) + R/2}{\Delta r})$, where $\text{round}(\cdot)$ rounds to the closest integer, and ξ is a multidimensional vector containing the curve parameters. It can be seen that MGRT is just the summation of $d(m, n)$ along the random-sampled transformation curve.

In our situation, the curve parameter vector ξ includes two parameters x and y, indicating the amplitude and phase of the sine function and $\phi(T_n; \xi)$ corresponds to the random-sampling curve in the range-slow time image $r(T_n) = y \cos \omega T_n + x \sin \omega T_n$. If a uniform sampling of the parameter domain is chosen, i.e.,

$$x_p = x_{\min} + p\Delta x, \quad p = 0, \ldots, P - 1 \tag{9}$$
$$y_q = y_{\min} + q\Delta y, \quad q = 0, \ldots, Q - 1 \tag{10}$$

where Δx and Δy are the discretization grids; $x_{\min} \leq \min_k(x_k)$ and $y_{\min} \leq \min_k(y_k)$ are the minimum value of parameters; $x_{\min} + (P-1)\Delta x \geq \max_k(x_k)$ and $y_{\min} + (Q-1)\Delta x \geq \max_k(y_k)$ are the maximum value of parameters. Then, the MGRT of the range-slow time image can be expressed as

$$D_{p,q} = D(x_p, y_q) = \sum_{n=0}^{N-1} d\left[\text{round}\left(\frac{r_{p,q}(T_n) + R/2}{\Delta r} \right), n \right] \tag{11}$$

where $r_{p,q}(T_n) = y_q \cos \omega T_n + x_p \sin \omega T_n$. Thus, one scatterer on the target, which is related to one curve in the range-slow time image, will result in one peak in the parameter domain. Finally, the image of the rotating target can be achieved corresponding to all the scatterers' coordinates. Due to the limited band of the signals used by the radar, some sidelobes are inevitable in the obtained range profile, and the main lobe has a certain width, which can not be reduced in the noncoherent processing. All these factors will affect the accuracy of the MGRT parameter domain, which reduces the resolution performance.

3.2. High Resolution Imaging by CS

Radar image demonstrates the locations and amplitudes of the strong target scattering centers, which represent the size and shape of the target. In practice, strong scattering centers usually take up only a fraction of whole image plane, while signals from weak scattering centers contribute little to image formation. Therefore, the echo signal can be approximated by a few strong scattering centers, which means sparse in this sense. If the locations of the target scatterers are present exactly at the grid points of Eqs. (9) and (10), we can reformat the signal model in Eq. (5) as

$$\begin{aligned}
s_r(r_m, T_n) &= \sum_{k=1}^{K} A_k \cdot B \cdot \text{sinc}\left[\frac{2B}{c}(r_m - r_k(T_n)) \right] \\
&\quad \cdot \exp\left(-j4\pi f_c \frac{r_k(T_n)}{c} \right) \\
&= \sum_{p=0}^{P-1} \sum_{q=0}^{Q-1} A_{p,q} \cdot \theta_{p,q}^{(m,n)}
\end{aligned} \tag{12}$$

with $\theta_{p,q}^{(m,n)} = B\text{sinc}[\frac{2B}{c}(r_m - r_{p,q}(T_n))] \exp(-j4\pi f_c \frac{r_{p,q}(T_n)}{c})$, where only the parameters $A_{p,q}$ at (x_p, y_q) corresponding to A_k at (x_k, y_k) are nonzero. Otherwise, if the locations of some target scatterers are not present exactly at the grid points, the number of nonzero $A_{p,q}$ will be slightly larger than K with some sidelobes. Therefore, by resolving $A_{p,q}$ which indicates the scatterer positions and reflectivities, we can generate the target image with high resolution.

In order to do so, we define the vectorization of $s_r(r_m, T_n)$ and $\theta_{p,q}^{(m,n)}$ (the result is denoted by $\mathbf{s}_r^{\text{vec}}$ and $\theta_{p,q}^{\text{vec}}$) by stacking their columns one underneath the other in sequence, i.e.,

$$\begin{aligned}
\mathbf{s}_r^{\text{vec}} &= [s_r(r_0, T_0), s_r(r_1, T_0), \ldots, s_r(r_{M-1}, T_0), \\
&\quad s_r(r_0, T_1), s_r(r_1, T_1), \ldots, s_r(r_{M-1}, T_1), \ldots, \\
&\quad s_r(r_0, T_{N-1}), s_r(r_1, T_{N-1}), \ldots, s_r(r_{M-1}, T_{N-1}),]^T \tag{13} \\
\theta_{p,q}^{\text{vec}} &= \left[\theta_{p,q}^{(0,0)}, \theta_{p,q}^{(1,0)}, \ldots, \theta_{p,q}^{(M-1,0)}, \right. \\
&\quad \theta_{p,q}^{(0,1)}, \theta_{p,q}^{(1,1)}, \ldots, \theta_{p,q}^{(M-1,1)}, \ldots, \\
&\quad \left. \theta_{p,q}^{(0,N-1)}, \theta_{p,q}^{(1,N-1)}, \ldots, \theta_{p,q}^{(M-1,N-1)} \right]^T \tag{14}
\end{aligned}$$

then Eq. (12) can be rewritten as the vector form as

$$\mathbf{s}_r^{\text{vec}} = \sum_{p=1}^{P} \sum_{q=1}^{Q} A_{p,q} \theta_{p,q}^{\text{vec}} = \boldsymbol{\Theta} \mathbf{a}^{vec} \tag{15}$$

where $\mathbf{\Theta} = [\theta_{0,0}^{\text{vec}}, \theta_{0,1}^{\text{vec}}, \ldots, \theta_{0,Q-1}^{\text{vec}}, \ldots, \theta_{P-1,Q-1}^{\text{vec}}] \in \mathrm{C}^{MN \times PQ}$ is the dictionary that respectively corresponds to all discretized spatial positions, and $\mathbf{a}^{\text{vec}} = [A_{0,0}, A_{0,1}, \ldots, A_{0,Q-1}, \ldots, A_{P-1,Q-1}]^T$ indicates the target image vector with complex reflectivities.

Because the number of dominant scatterers is much smaller than the number of discretized spatial positions, there are some large coefficients and many small coefficients in $\mathbf{a}^{\text{vec}}$, which can be deemed as a sparse vector. When MN is smaller than PQ and on the order of K, Eq. (15) can be represented as a typical CS problem. By further taking into consideration the perturbation $\mathbf{e}$ in the practical measurement vector, the following basis pursuit denoising (BPDN) problem can be introduced to generate the target image

$$\hat{\mathbf{a}}^{\text{vec}} = \arg\min_{\mathbf{a}^{\text{vec}}} \|\mathbf{a}^{\text{vec}}\|_1 \text{ subject to } \|\mathbf{s}_r^{\text{vec}} - \mathbf{\Theta}\mathbf{a}^{\text{vec}}\|_2 \leq \varepsilon \tag{16}$$

where ε is the fitting error threshold satisfying $\varepsilon = \|\mathbf{e}\|_2$, $\|\cdot\|_p$ denotes the l_p-norm.

3.3. SDD-CS Processing Scheme for Wideband RPRI Radar

Although the high resolution target image can be obtained by resolving Eq. (16), the large-scale dictionary will result in high computational complexity. As we have already achieved the low resolution image $D_{p,q}$ by the MGRT, the dictionary can be scaled down according to the strong scattering areas, which contains almost all the scatterers. The problem in determining the strong scattering areas is shifted to discriminating image cells containing signal components from noise range cells, which could be treated as a problem of target detection in the 2-D image domain.

Inspired by an ordered-statistics constant-false-alarm-rate (CFAR) detector [28] as well as noise level estimation in [22], we can first order all image cells by their energy and determine the cells with largest energy as signal cells and the rest as noise samples. The lower threshold for the mean energy of image cells to select signal cells is given as

$$\eta = E_m + \sqrt{\frac{1}{PQ-1}\sum_{p=1}^{P}\sum_{q=1}^{Q}\left(D_{p,q}^2 - E_m\right)^2} \tag{17}$$

where $E_m = \frac{1}{PQ}\sum_{p=1}^{P}\sum_{q=1}^{Q}D_{p,q}^2$ is the mean energy of all cells available. When the energy of a image cell is below the threshold, it is determined as a pure noise cell. On the contrary, when the energy of an image cell is above the threshold, it is determined as a strong scattering cell. This energy-based threshold is composed of two terms: the energy mean and the square root of energy variance. Clearly, the threshold is adjusted with SNR adaptively, and because the energy-based threshold is independent of the statistics of clutter noise, it should be applied well in different situations. Even so, in some extremely low SNR cases, it is helpful to take the statistics of clutter noise into account, and other threshold with CFAR [29] in radar iamging are supportive to select strong scattering cells.

Consequently, considering that the $(Qp + q + 1)$th element of $\mathbf{a}^{\text{vec}}$ corresponds to the image data from the possible scatterer located at (p, q)th discretized position in the target spatial domain, we can obtain the index set indicating the positions of those strong areas as

$$\Lambda = \left\{Qp + q + 1 | D_{p,q}^2 \geq \eta\right\} \tag{18}$$

Assume that the cardinality of Λ is L which is smaller than PQ, then the scale-down signal model and solution which correspond to Eqs. (15) and (16) can be represented as

$$\mathbf{s}_\Omega^{vec} = \mathbf{\Psi}\mathbf{s}_r^{\text{vec}} = \mathbf{\Psi}\mathbf{\Theta}_\Lambda \mathbf{a}_\Lambda^{vec} \tag{19}$$

$$\hat{\mathbf{a}}_\Lambda^{vec} = \arg\min_{\mathbf{a}_\Lambda^{vec}} \|\mathbf{a}_\Lambda^{vec}\|_1 \text{ subject to } \|\mathbf{s}_\Omega^{vec} - \mathbf{\Psi}\mathbf{\Theta}_\Lambda \mathbf{a}_\Lambda^{vec}\|_2 \leq \varepsilon_\Lambda \tag{20}$$

where $\mathbf{\Psi}$ is the $S \times MN$ matrix extracting the sampled coordinates in $\Omega \subset \{1, 2, \ldots, MN\}$ which is a random subset of cardinality $K < S < \min(L, MN)$, $(\cdot)_\Lambda$ denotes the columns or elements in a matrix or vector indexed within Λ and $\varepsilon_\Lambda = \sqrt{S/(MN)}\varepsilon$. It can be seen form Eq. (19) that the dimension of scale-down-dictionary $\mathbf{\Psi}\mathbf{\Theta}_\Lambda$ is $S \times L$, which is smaller than $MN \times PQ$. Thus the computational complexity is also much lower. Finally, the detailed processing steps for wideband SDD-CS imaging of fast rotating targets is given in Fig. 3.
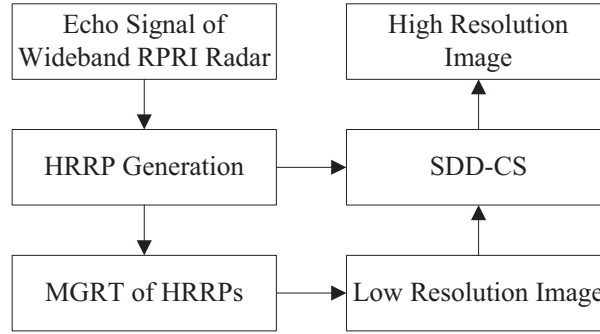
Figure 3. Processing steps for wideband SDD-CS imaging of fast rotating targets.

4. COMPLEMENTARY ISSUES TO SDD-CS

4.1. Analysis of Resolution Performance

It has already been pointed out in [30] that the resolution performance of CS-based imaging algorithm is determined by the discretization grid of the target spatial domain. In our situation, high resolution comes from smaller values of Δx and Δy. This is different from the conventional imaging approaches, where the image resolution is mainly related with the point spread function [31]. However, the values of Δx and Δy cannot infinitely decrease, because the mutual coherence of the dictionaries will be too large to solve the BPDN problem. Thus, it can be concluded that the actual resolution ability of CS-based algorithm is highly related with the performance of exact recovery, which is determined by the complex factors consisting of the dictionary characteristics, the target sparsity as well as the sparse recovery algorithms. Although there are many issues concerning the exact recovery conditions for various algorithms based on restricted isometry property [32], mutual coherence [33] or unique representation property [34], etc., all these conditions are somewhat conservative in practical situations, and good recovery quality is possible for a larger class of signal models than the conditions would suggest. Therefore, further investigation is still required on this open problem as well as the resolution performance of CS-based approaches.

4.2. Computational Complexity

As shown in Table 1, we will present the computational complexity of the proposed SDD-CS scheme for wideband radar imaging, as well as the CBP-based and direct-CS-based cases. Assume that the CVX toolbox in [35] is used to resolve the BPDN problem, the computational cost of SDD-CS scheme is mainly contributed by MGRT ($O(PQN)$) and SDD-CS ($O(L^3)$). For comparison, we also present the computational cost of wideband CBP given by $O(2PQMN)$, which is much lower. Even now, compared with the direct-CS scheme which requires $O(P^3Q^3)$, the SDD-CS scheme shows great superiority especially when the strong scattering areas are smaller. Therefore, it can be concluded that the proposed SDD-CS scheme outperforms the traditional algorithms from perspectives of both computational cost and precision performance, which will be further verified in Section 5.

Table 1. Time computational cost comparison of the THREE Algorithms.

Algorithms	Computational Cost
SDD-CS	$O(PQN) + O(L^3)$
CBP	$O(2PQMN)$
Direct-CS	$O(P^3Q^3)$

5. NUMERICAL SIMULATIONS

In this section, the feasibility and performance of the proposed SDD-CS scheme for wideband radar imaging of fast rotating targets are tested by comparing to both GRT (or MGRT) and CBP algorithms. Our simulations are performed in MATLAB7 environment using a Pentium (R) 4 CPU 3.00 GHz processor with 1 GB of memory and under Microsoft Windows XP operating system. In all the simulations, the target rotation frequency is assumed to be exactly obtained by some existing approaches and parameters of each algorithm are set manually for sound results.

5.1. Wideband FPRI Imaging of Fast Rotating Targets

The carrier frequency of the FPRI radar is assumed to be $f_c = 10$ GHz, and the wavelength is $\lambda = 0.03$ m. The pulse width and bandwidth of transmitted wideband chirp signal are $T = 50\,\mu$s, $B = 500$ MHz, which gives a range resolution of 0.3 m. The scatterer distribution is depicted in Fig. 4(a), where the back-scattering coefficients are the same for all scatterers. The target rotates with a frequency of $f_{rot} = 20$ Hz and the maximum rotation radius is about 1.15 m. According to the conclucion in [23], the required PRF for the CBP method is 19.268 kHz. As pointed out in [3], for practical use of wideband radar, the required PRF can be much lower than its theoretical value. In this simulation, the PRF is set to be 200 Hz, which is low enough to generate aliasing image. The imaging interval is 0.5 s, and the
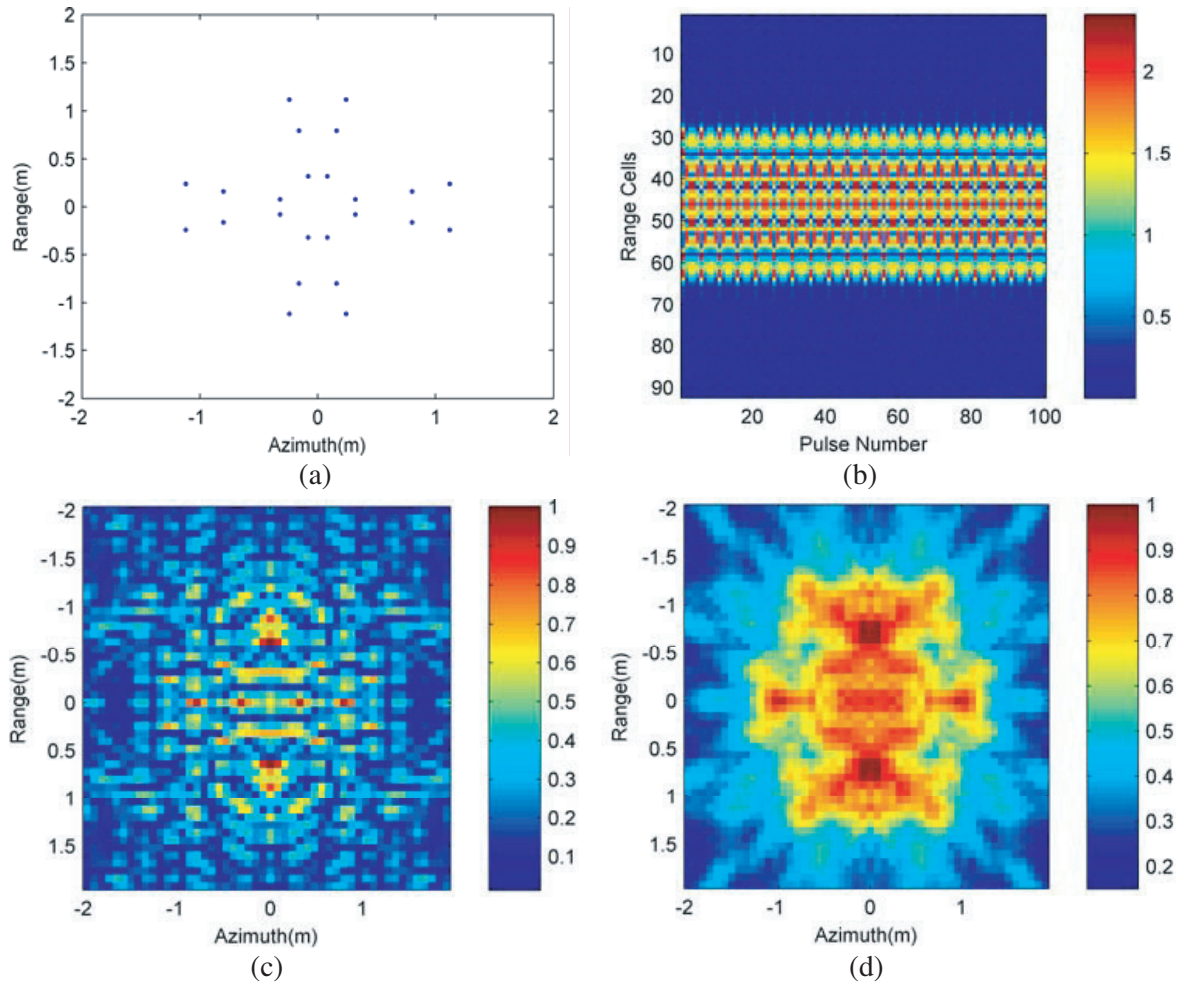

Figure 4. Wideband FPRI imaging results of fast rotating targets. (a) Scatterer distribution. (b) Aligned HRRPs. (c) CBP imaging result. (d) GRT imaging result.

number of azimuth samples is $N = 100$. The scope of target scene is set to $(-2m, 2m) \times (-2m, 2m)$ and the sampling interval in 0.08 m.

We add complex-valued white Gaussian noise to target echoes to obtain the SNR of 10 dB and Fig. 4(b) shows the obtained HRRPs with $M = 92$ range cells for all the pulses after range compression. Based on the HRRPs, the high and low resolution target images can be generated by the CBP and GRT algorithms as shown in Figs. 4(c)–(d), form which it can be seen that both of the images suffer from serious aliasing. Those spurious peaks are caused by the interference among sidelobes, which may also shadow the imaging of real scatterers.

5.2. Wideband RPRI Imaging of Fast Rotating Targets

In order to suppress the aliasing effect, we can use the RPRI radar, in which all the radar parameters are unchanged except that the $N = 100$ pulses are transmitted during the dwell time in a random jittering way. Fig. 5 presents the transmitting slow time of each pulse for the FPRI and RPRI schemes. The corresponding HRRPs are shown in Fig. 6(a), based on which the target image generated by the CBP and MGRT algorithms are given in Figs. 6(b)–(c). It can be seen that due to the random jittering slow time, the aliasing effect can be well suppressed and the target structure can be roughly formed. However, on the one hand, although the CBP algorithm can obtain the well focused target image, it always suffers from high sidelobe pedestal and computational complexity. On the other hand, for the MGRT algorithm, the image resolution performance is much poorer and we can hardly distinguish the scatterers.
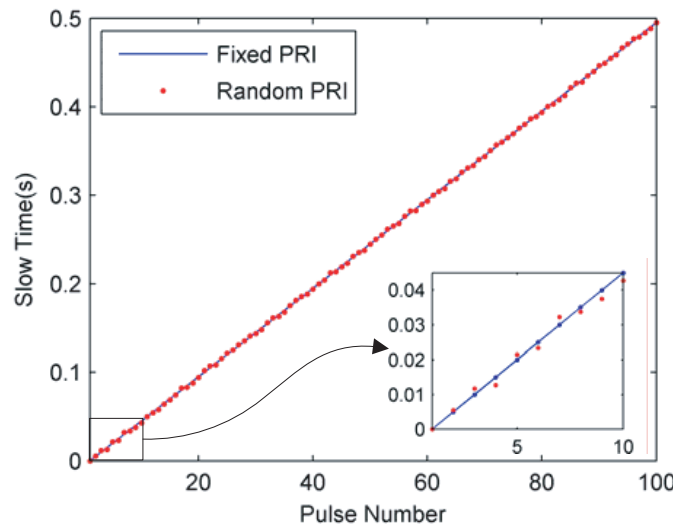

Figure 5. Wideband RPRI radar worked in a jittering way.

As the direct CS processing with the large-scale dictionary suffers from high computational complexity and some existing toolbox even cannot deal with the $PQ = 2500$ atoms in our situation, here we only apply the SDD-CS scheme to wideband RPRI radar imaging. In order to do so, we firstly perform CFAR detection on the low resolution image generated by MGRT to obtain those strong scattering areas. As shown in Fig. 6(d), we can observe that the strong scattering areas can always cover the real scatterers because the image is with low resolution and no aliasing. Then the dictionary is scaled down in both row and column. The scale down of dictionary rows is performed by traditional random sampling of the HRRPs in both range cells and slow time [19], as shown in Fig. 6(e). Considering that the number of scatterers is 24, the random sampling number is set to be $S = 100$. Furthermore, the dictionary columns are scaled down by reserving the atoms corresponding to the strong scattering areas and the number is $L = 497$ in this situation. Finally, the scatterer positions can be estimated accurately by the CS approach as shown in Fig. 6(f), which has high resolution and hardly any sidelobes.
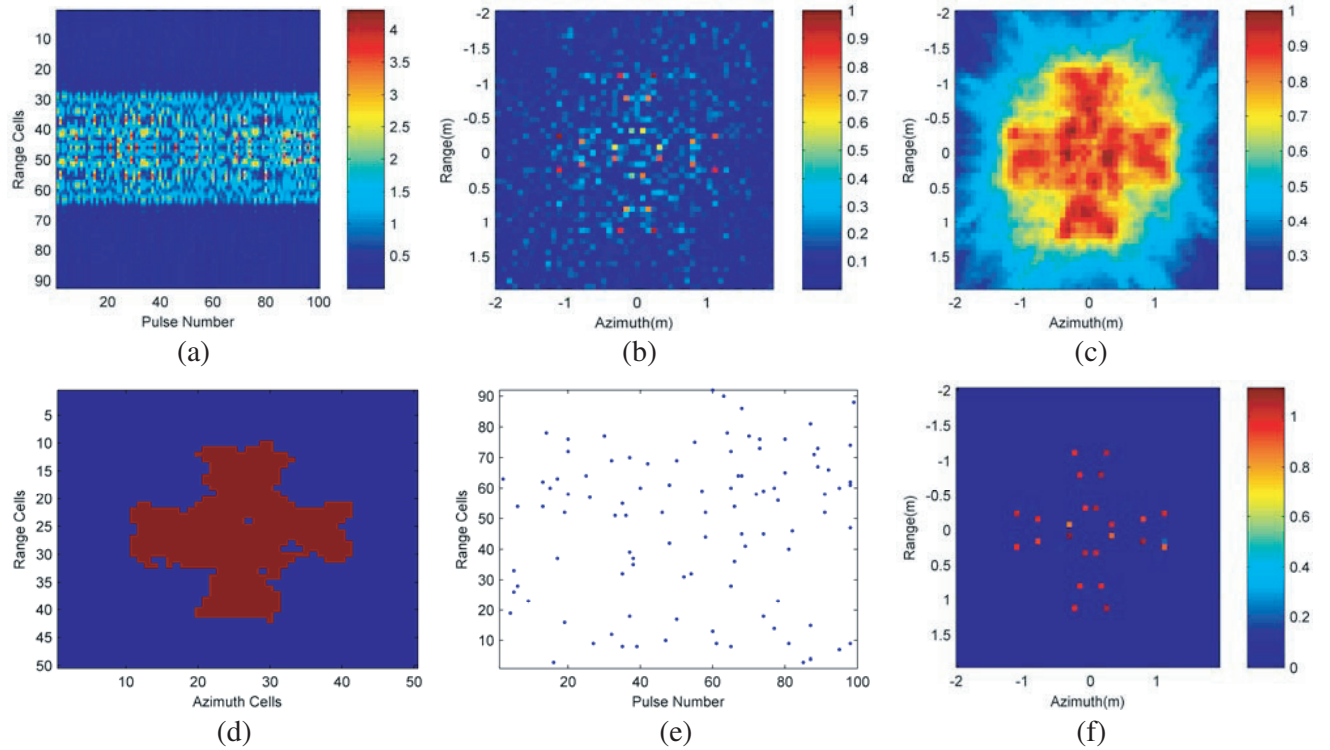
Figure 6. Wideband RPRI imaging results of fast rotating targets. (a) Aligned HRRPs. (b) CBP imaging result. (c) MGRT imaging result. (d) Strong scattering areas. (e) Random sampling in both range cells and slow time. (f) SDD-CS imaging result.

Therefore, it can be concluded that in our case of sparse point targets, the number of measurements can be reduced to only 1/92 or even less of the traditional samples and the target scene can be reduced to 1/5 of the traditional atoms, both of which greatly reduce the computational cost. Furthermore, the results of the SDD-CS imaging scheme are even much better than the traditional results of the whole data. The main reason is that the sparse information of the targets is considered in the CS-based imaging scheme, while the traditional imaging method uses no *a priori* information of the targets.

6. CONCLUSION

In this paper, the RPRI signal associated with the CS theory is introduced for aliasing reduction to obtain well-focused image of extremely fast rotating targets in wideband radar. The SDD-CS processing scheme is applied to lower the computational complexity. Firstly, the MGRT is applied on the range-slow time domain to generate the low resolution image for wideband RPRI radar. Then the dictionary is scaled down by reserving the atoms corresponding to those strong scattering areas. Simulations are performed to test the performance of the SDD-CS scheme, the results of which indicate that it can achieve preferable images with no aliasing as well as acceptable computational cost. Now the wideband RPRI radar is under developing, and the proposed scheme will be applied to the experimental data in our future work.

ACKNOWLEDGMENT

REFERENCES

1. Wang, Q., M. D. Xing, G. Lu, and Z. Bao, "High-resolution three-dimensional radar imaging for rapidly spinning targets," *IEEE Transactions on Geoscience and Remote Sensing*, Vol. 46, No. 1, 22–30, Jan. 2008.

2. Zhang, Q., T. S. Yeo, H. S. Tan, and Y. Luo, "Imaging of a moving target with rotating parts based on the Hough transform," *IEEE Transactions on Geoscience and Remote Sensing*, Vol. 46, No. 1, 291–299, Jan. 2008.

3. Bai, X., F. Zhou, M. Xing, and Z. Bao, "High resolution ISAR imaging of targets with rotating parts," *IEEE Transactions on Aerospace and Electronic Systems*, Vol. 47, No. 4, 2534–2543, Oct. 2011.

4. Bai, X., M. Xing, F. Zhou, and Z. Bao, "High-resolution three-dimensional imaging of spinning space debris," *IEEE Transactions on Geoscience and Remote Sensing*, Vol. 47, No. 7, 2352–2362, Jul. 2009.

5. Huo, K., Y. Liu, J. Hu, W. Jiang, and X. Li, "A novel imaging method for fast rotating targets based on the segmental pseudo Keystone transform," *IEEE Transaction on Geoscience and Remote Sensing*, Vol. 39, No. 4, 1464–1472, Apr. 2011.

6. Luo, Y., Q. Zhang, C. Qiu, X. Liang, and K. Li, "Micro-Doppler effect analysis and feature extraction in ISAR imaging with stepped-frequency chirp signals," *IEEE Transactions on Geoscience and Remote Sensing*, Vol. 48, No. 4, 2087–2098, Apr. 2010.

7. Cook, C. E. and M. Bernfeld, *Radar Signals: An Introduction to Theory and Application*, Academic Press, New York, 1967.

8. Kaveh, M. and G. R. Cooper, "Average ambiguity function for a randomly staggered pulse sequence," *IEEE Transactions on Aerospace and Electronic Systems*, Vol. 12, No. 3, 410–413, May 1976.

9. Vergara-Dominguez, L., "Analysis of the digital MTI filter with random PRI," *IEE Proceedings — F*, Vol. 140, No. 2, 129–137, Apr. 1993.

10. Benjamin, R., "Form of Doppler processing for radars of random p.r.i. and r.f.," *Electronics Letters*, Vol. 15, No. 24, 782, Nov. 1979.

11. Candès, E., J. Romberg, and T. Tao, "Robust uncertainty principles: Exact signal reconstruction from highly incomplete frequency information," *IEEE Transactions on Information Theory*, Vol. 52, No. 2, 489–509, Feb. 2006.

12. Candès, E. and T. Tao, "Near optimal signal recovery from random projections: Universal encoding strategies?," *IEEE Transactions on Information Theory*, Vol. 52, No. 12, 5406–5425, Dec. 2006.

13. Donoho, D., "Compressed sensing," *IEEE Transactions on Information Theory*, Vol. 52, No. 4, 1289–1306, Apr. 2006.

14. Bourguignon, S., H. Carfantan, and J. Idier, "A sparsity-based method for the estimation of spectral lines from irregularly sampled data," *IEEE Journal of Selected Topics in Signal Processing*, Vol. 1, No. 4, 575–585, Dec. 2007.

15. Stoica, P., P. Babu, and J. Li, "New method of sparse parameter estimation in separable models and its use for spectral analysis of irregularly sampled data," *IEEE Transactions on Signal Processing*, Vol. 59, No. 1, 35–47, Jan. 2011.

16. Patel, V. M., G. R. Easley, D. M. Healy, Jr., and R. Chellappa, "Compressed synthetic aperture radar," *IEEE Journal of Selected Topics in Signal Processing*, Vol. 4, No. 2, 244–254, Apr. 2010.

17. Liu, Z., X. Z. Wei, and X. Li, "Adaptive clutter suppression for airborne random pulse repetition interval radar based on compressed sensing," *Progress In Electromagnetics Research*, Vol. 128, 291–311, 2012.

18. Liu, Z., X. Z. Wei, and X. Li, "Aliasing-free moving target detection in random pulse repetition interval radar based on compressed sensing," *IEEE Sensors Journal*, Vol. 13, No. 7, 2523–2534, Jul. 2013.

19. Alonso, M. T., P. López-Dekker, and J. J. Mallorquí, "A novel strategy for radar imaging based on compressive sensing," *IEEE Transactions on Geoscience and Remote Sensing*, Vol. 48, No. 12,

4285–4295, Dec. 2010.

20. Wei, S. J., X. L. Zhang, J. Shi, and G. Xiang, "Sparse reconstruction for SAR imaging based on compressed sensing," *Progress In Electromagnetics Research*, vol. 109, 63–81, 2010.

21. Wei, S. J., X. L. Zhang, and J. Shi, "Linear array SAR imaging via compressed sensing," *Progress In Electromagnetics Research*, Vol. 117, 299–319, Jun. 2011.

22. Zhang, L., M. Xing, C. Qiu, J. Li, J. Sheng, Y. Li, et al., "Resolution enhancement for inversed synthetic aperture radar imaging under low SNR via improved compressive sensing," *IEEE Transactions on Geoscience and Remote Sensing*, Vol. 48, No. 10, 3824–3838, Oct. 2010.

23. You, P., Z. Liu, X. Wei, H. Wang, and X. Li, "Aliasing-free high resolution imaging of fast rotating targets with narrowband radar," *Journal of Central South University*, Vol. 21, 1842–1851, 2014.

24. Liu, Z., X. Wei, and X. Li, "Aliasing-free micro-Doppler analysis based on short-time compressed sensing," *IET Signal Processing*, Vol. 8, No. 2, 176–187, 2014.

25. Xing, M. D., R. B. Wu, J. Q. Lan, and Z. Bao, "Migration through resolution cell compensation in ISAR imaging," *IEEE Geoscience and Remote Sensing Letters*, Vol. 1, No. 2, 141–144, Apr. 2004.

26. Bai, X. R., G. C. Sun, Q. S. Wu, M. D. Xing, and Z. Bao, "Narrow-band radar imaging of spinning targets," *Sci. China Inf. Sci.*, Vol. 54, No. 4, 873–883, Apr. 2011.

27. Hansen, K. V. and P. A. Toft, "Fast curve estimation using preconditioned generalized Radon transform," *IEEE Transactions on Image Processing*, Vol. 5, No. 12, 1651–1661, Dec. 1996.

28. Rohling, H., "Radar CFAR thresholding in clutter and multiple target situations," *IEEE Transactions on Aerospace and Electronic Systems*, Vol. 19, No. 4, 608–621, Jul. 1983.

29. Martorella, M., N. Acito, and F. Berizzi, "Statistical CLEAN technique for ISAR imaging," *IEEE Transactions on Geoscience and Remote Sensing*, Vol. 45, No. 11, 3552–3560, Nov. 2007.

30. Li, G., H. Zhang, and X. Wang, "ISAR 2-D imaging of uniformly rotating targets via matching pursuit," *IEEE Transactions on Aerospace and Electronic Systems*, Vol. 48, No. 2, 1838–1846, Apr. 2012.

31. Zhang, L., M. Xing, C. Qiu, J. Li, and Z. Bao, "Achieving higher resolution ISAR imaging with limited pulses via compressed sampling," *IEEE Geoscience and Remote Sensing Letters*, Vol. 6, No. 3, 567–571, Jul. 2009.

32. E. Candès, J. Romberg, and T. Tao, "Stable signal recovery from incomplete and inaccurate measurements," *Communications on Pure and Applied Mathematics*, Vol. 59, No. 8, 1207–1223, Aug. 2006.

33. Donoho, D. L., M. Elad, and V. N. Temlyakov, "Stable recovery of sparse overcomplete representations in the presence of noise," *IEEE Transactions on Information Theory*, Vol. 52, No. 1, 6–18, Jan. 2006.

34. Babaie-Zadeh, M. and C. Jutten, "On the stable recovery of the sparsest overcomplete representations in presence of noise," *IEEE Transactions on Signal Processing*, Vol. 58, No. 10, 5396–5400, Oct. 2010.

35. Grant, M. and S. Boyd, "CVX: Matlab software for disciplined convex programming," http://stanford.edu/~boyd/cvxCVX, 2008.